nature nanotechnology

Letter

https://doi.org/10.1038/s41565-022-01217-x

Chirality-dependent unidirectional routing of WS_2 valley photons in a nanocircuit

Received: 2 June 2022

Accepted: 19 August 2022

Published online: 3 October 2022

Check for updates

Yang Chen[1,2,3,10], Shuhang Qian[1,4,10], Kai Wang[1,4] ✉, Xiangyuan Xing[1,4], Andrew Wee[5], Kian Ping Loh[6], Bing Wang[1,4], Dong Wu[2], Jiaru Chu[2], Andrea Alu[7,8], Peixiang Lu[1,4,9] ✉ and Cheng-Wei Qiu[3] ✉

Valleytronics is a promising candidate to address low-energy signal transport on chip, leveraging the valley pseudospin of electrons as a new degree of freedom to encode, process and store information[1–7]. However, valley-carrier nanocircuitry is still elusive, because it essentially requires valley transport that overcomes three simultaneous challenges: high fidelity, high directionality and room-temperature operation. Here we experimentally demonstrate a nanophotonic circuit that can route valley indices of a WS_2 monolayer unidirectionally via the chirality of photons. Two propagating modes are supported in the gap area of the circuit and interfere with each other to generate beating patterns, which exhibit complementary profiles for circular dipoles of different handedness. Based on the spin-dependent beating patterns, we showcase valley fidelity of chiral photons up to 98%, and the circulation directionality is measured to be 0.44 ± 0.04 at room temperature. The proposed nanocircuit can not only enable the construction of large-scale valleytronic networks but also serve as an interactive interface to integrate valleytronics[3–5], spintronics[8–10] and integrated photonics[11–13], opening new possibilities for hybrid spin-valley-photon ecosystems at the nanoscale.

Unidirectional transport of information carriers is essential for modern information and communication technology and has been realized for acoustic waves[14], radio frequency signals[15] and quantum bits[16]. Particularly in electronics, the gyrator that only allows radio frequency signals to exit through the port directly after the one they enter is among the most fundamental elements to construct electronic networks[17]. Recently, the valley pseudospin of electrons, as a new degree of freedom (DOF), has been harnessed as an information carrier, potentially exhibiting higher processing speed, lower power consumption and less heat production than conventional electronics. However, the short lifetimes of excitons and valley polarization, as well as the low mobility of valley materials, have seriously hindered the transport of the valley DOF (refs. [3–5]), let alone the unidirectional circulation of valleys.

One way to overcome the valley transport problem is to convert the valley indices of excitons into the chirality of photons[18–20], which can propagate over a long distance. The previously reported approaches employing spin-momentum locked waveguides have achieved the

[1]Wuhan National Laboratory for Optoelectronics and School of Physics, Huazhong University of Science and Technology, Wuhan, China. [2]Chinese Academy of Sciences Key Laboratory of Mechanical Behavior and Design of Materials, Department of Precision Machinery and Precision Instrumentation, University of Science and Technology of China, Hefei, China. [3]Department of Electrical and Computer Engineering, National University of Singapore, Kent Ridge, Singapore. [4]Optics Valley Laboratory, Wuhan, China. [5]Department of Physics, National University of Singapore, Kent Ridge, Singapore. [6]Department of Chemistry, National University of Singapore, Kent Ridge, Singapore. [7]Photonics Initiative, Advanced Science Research Center, City University of New York, New York, NY, USA. [8]Physics Program, Graduate Center of the City University of New York, New York, NY, USA. [9]Hubei Key Laboratory of Optical Information and Pattern Recognition, Wuhan Institute of Technology, Wuhan, China. [10]These authors contributed equally: Yang Chen, Shuhang Qian. ✉e-mail: kale_wong@hust.edu.cn; lupeixiang@hust.edu.cn; chengwei.qiu@nus.edu.sg

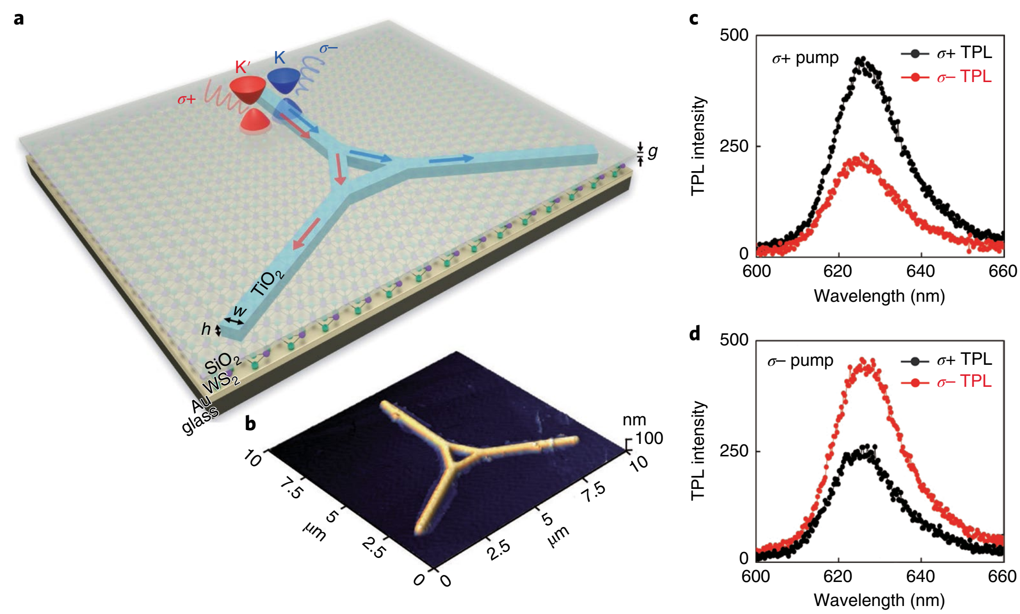

Fig. 1 | Schematic of the nanophotonic circuit. a, Illustration of the nanocircuit enabling the directional routing of K and K′ valleys. The width and height of the waveguide are $w = 240$ nm and $h = 100$ nm. The thickness of the SiO_2 film is $g = 20$ nm. **b**, An atomic force microscopy image of a fabricated circuit sample. **c**,**d**, Spin-resolved TPL spectra for a bare WS_2 monolayer under σ+ (**c**) and σ− (**d**) excitations.

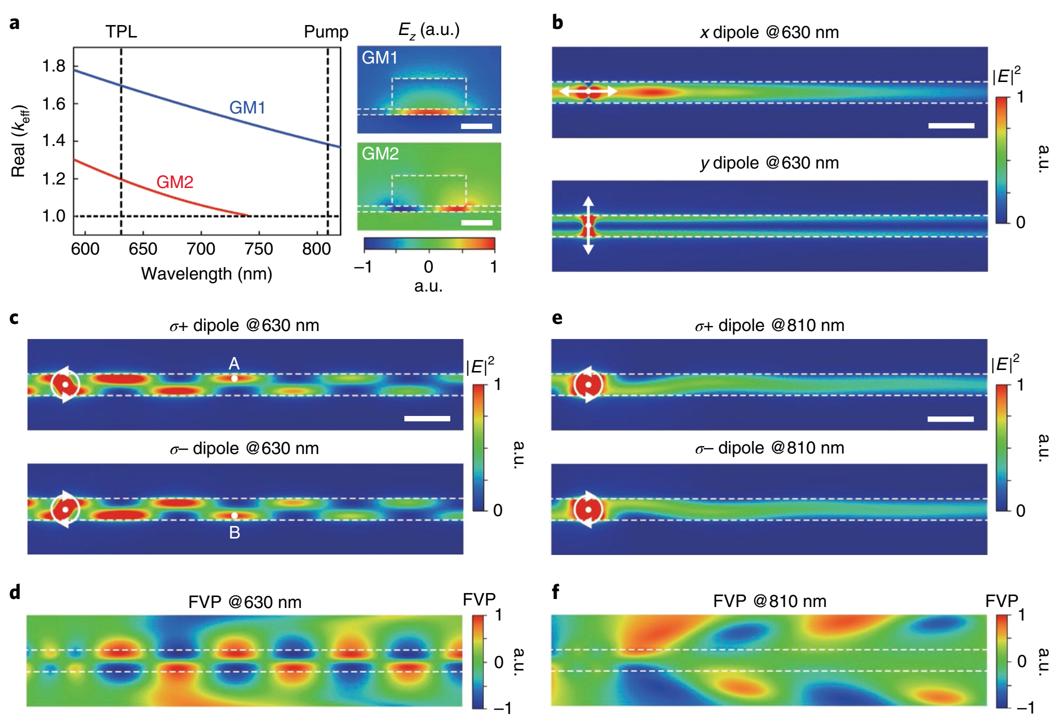

Fig. 2 | Principle of valley preservation. a, The real parts of effective wavevectors for GM1 and GM2 at different wavelengths. The cross-section E_z distributions of GM1 and GM2 are plotted on the right. Scale bar, 500 nm. **b**, Normalized electric field intensity distributions in the gap of the waveguide excited by *x*- and *y*-polarized dipoles at 630 nm. **c**,**e**, Normalized electric field intensity distributions for σ+ and σ− dipoles at wavelengths of 630 nm (**c**) and 810 nm (**e**). Scale bars, 100 nm. **d**,**f**, Calculated FVP profiles (FVP = $(|E_{\sigma+}|^2 - |E_{\sigma-}|^2) / (|E_{\sigma+}|^2 + |E_{\sigma-}|^2)$) at wavelengths of 630 nm (**d**) and 810 nm (**f**).

separation of valley indices[21–25]. However, they cannot be utilized for valley circulation, because the two valleys are separately transferred to two counter-propagating waveguide modes and hence the valley DOF is lost for a single waveguide, leaving no space for the further processing. Apparently, the key to realizing the function of valleytronic gyrators is to preserve the valley DOF during photon propagation, that is, photons corresponding to different valleys are conveyed towards a single optical fibre without mutual disturbance. This can then be exploited for valley circulation.

As illustrated in Fig. 1a, the nanocircuit is based on hybrid WS_2-in-gap waveguides composed of TiO_2 nanowires separated from a gold surface by a nanoscale SiO_2 gap, and a WS_2 monolayer is sandwiched between the gold surface and the SiO_2 layer. Two-dimensional transition-metal dichalcogenides, such as MoS_2 and WS_2, have been considered as promising

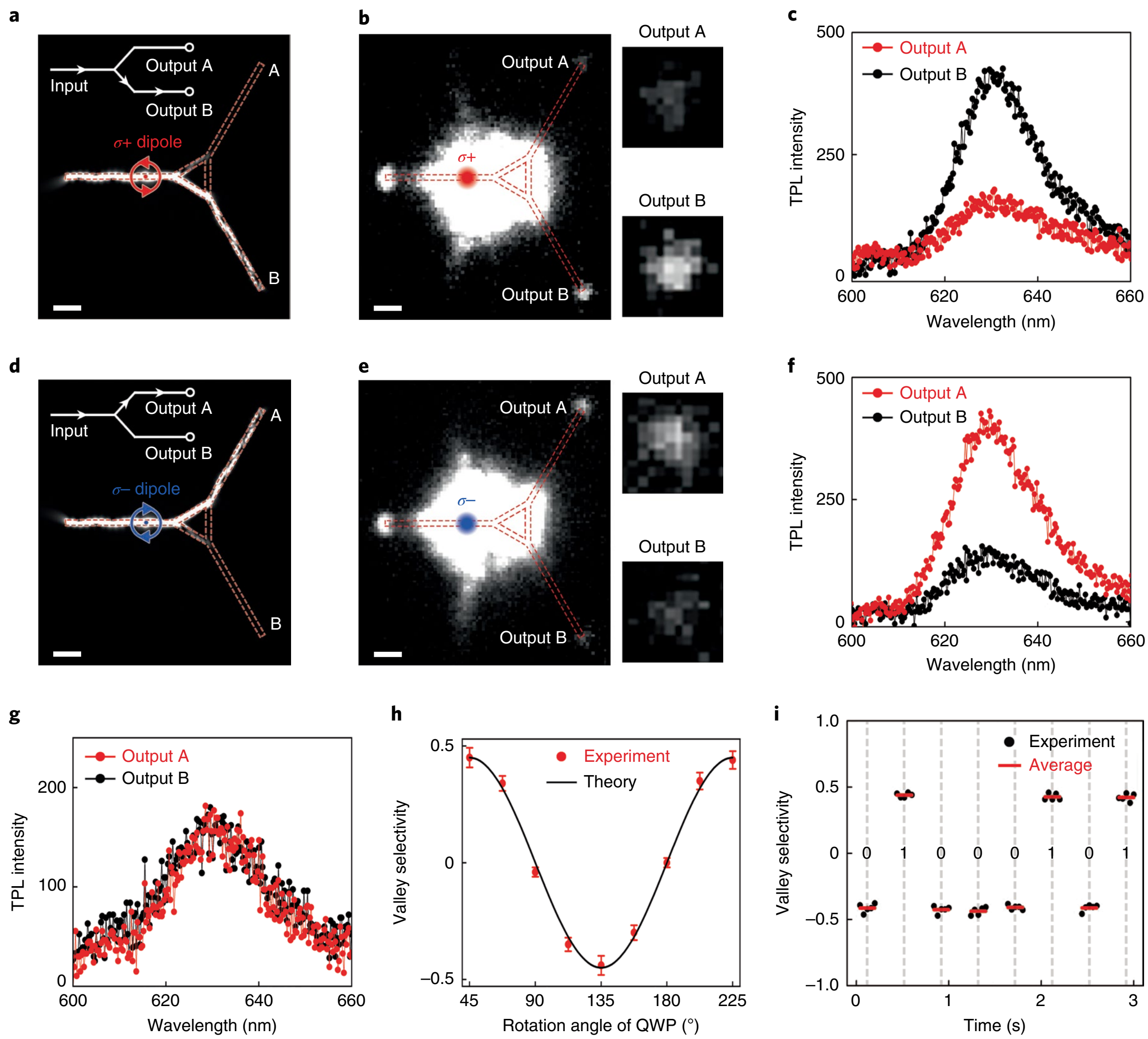

Fig. 3 | Demonstration of directional valley router. **a**,**d**, Simulated electric field intensity distributions of the valley router when excited by a $\sigma+$ (**a**) or $\sigma-$ (**d**) dipole at 630 nm. Scale bars, 1 µm. **b**,**e**, Captured TPL images of the valley router when excited by a focused pump laser of $\sigma+$ (**b**) or $\sigma-$ (**e**) polarization. Scale bars, 1 µm. The zoomed-in images of output ports A and B are shown on the right. **c**,**f**,**g**, TPL spectra measured from ports A and B for $\sigma+$ (**c**), $\sigma-$ a.u. (**f**) or linearly polarized a.u. (**g**) excitations a.u. **h**, Experimental and theoretical VSs as a function of the rotation angle φ of the QWP. The error bars indicate the standard deviation of multiple measurements. **i**, Time sequence of measured VS for the binary code of 'E'.

materials for valleytronics due to their electronic structures supporting two degenerate yet inequivalent valleys at the K and K′ points of the Brillouin zone[26–28]. The nanocircuit can be mass produced by nanofabrication processes (see 'Sample fabrication' in the Methods and Supplementary Fig. 1). The atomic force microscopy and optical microscopy images of nanocircuit samples are shown in Fig. 1b and Supplementary Fig. 2, respectively. A Ti:sapphire femtosecond laser at 810 nm wavelength is utilized to excite the two-photon luminescence (TPL) of the WS_2 monolayer. The pump power is about 22 mW before illuminating on the WS_2 monolayer, corresponding to a power density of 0.7 MW cm^{-2}. Governed by the valley-dependent optical selection rule, excitons at the K′ valley, once pumped from the ground state to the $2p_+$ state through the absorption of two $\sigma+$ fundamental photons, will experience an interexciton relaxation from the $2p_+$ to the $1s$ state and then emit a $\sigma+$ photon at 630 nm wavelength[29]. Similarly, K valley excitons pumped by two-photon $\sigma-$ excitation will generate $\sigma-$ TPL emission. This non-linear selection rule is experimentally verified by spin-resolved TPL spectra measured from a bare WS_2 monolayer (Fig. 1c,d), where the helicity of TPL basically follows that of the excitation light. The valley polarization $P_v = (I_{\sigma+} - I_{\sigma-})/(I_{\sigma+} + I_{\sigma-})$ is measured to be 0.38 and −0.34 for $\sigma+$ and $\sigma-$ excitations, respectively, where $I_{\sigma+}$ and $I_{\sigma-}$ are the TPL intensities of $\sigma+$ and $\sigma-$ polarizations, respectively.

When a WS_2 monolayer is integrated into the hybrid waveguide, its TPL emission will couple to the waveguide mode with the emission rate modified by the Purcell effect[30,31]. The unique nanowire-on-mirror waveguide configuration enables a class of hybrid modes strongly confined in the gap area beneath the TiO_2 nanowire, known as gap modes (GMs)[32]. GMs are formed by the near-field coupling between the guided photonic modes of the nanowire and the surface plasmon polaritons of the gold surface[32], characteristic of both strong mode confinement and a large propagation distance. The propagation distance is measured in Supplementary Section 2. At the resonant wavelength of TPL (about 630 nm), two propagating GMs are supported (Fig. 2a). The first-order GM (GM1) exhibits symmetric mode profiles as revealed by the E_z field distributions, while the second-order GM (GM2) presents antisymmetric profiles (Fig. 2a). If an x-polarized electric dipole emitting at 630 nm is positioned at the centre of the gap area, it can only launch GM1 due to symmetry, while a y-polarized dipole can only excite GM2 (Fig. 2b).

When in-plane $\sigma+$ and $\sigma-$ circular dipoles are considered, corresponding to the circularly polarized TPL emission from K′ and K valleys of the WS_2 monolayer, GM1 and GM2 are simultaneously excited. Owing to the existence of a wavevector mismatch $\Delta k = k_{GM1} - k_{GM2}$ between the two GMs, a beating pattern is created by mode interference, with

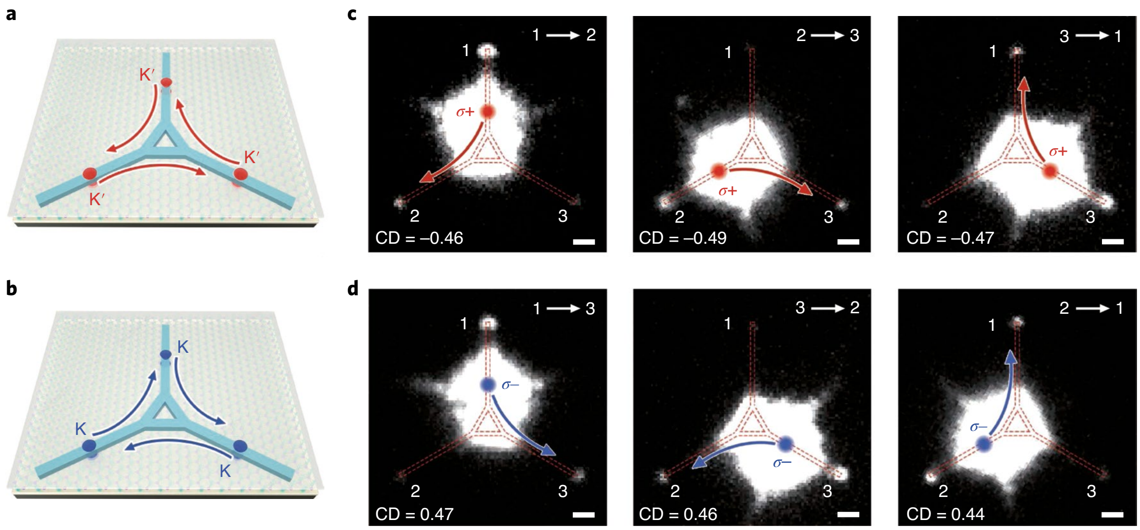

Fig. 4 | Unidirectional valley circulation among multiple channels. a–d, Schematic illustrations (**a**,**b**) and measured TPL images (**c**,**d**) of the circuitry enabling the unidirectional routing of valley information. The routing is counterclockwise for K′ valley excitons (**a**,**c**) and clockwise for K valley excitons (**b**,**d**). Scale bars, 1 μm.

a beating length $l = 2\pi/\Delta k = 1{,}261$ nm, which is consistent with simulation results (Fig. 2c). The beating pattern exhibits complementary field distributions for the σ+ and σ− dipoles. Photons appearing at point A exclusively originate from the σ+ dipole, while photons emergent at point B on the other side come from the σ− dipole. In this way, the valley pseudospin of electrons is converted to the chirality of beating waveguide modes, and the fidelity of valley preservation (FVP), quantitatively evaluated by $\mathrm{FVP} = (|E_{\sigma+}|^2 - |E_{\sigma-}|^2) / (|E_{\sigma+}|^2 + |E_{\sigma-}|^2)$, can be up to 98%, close to the perfect value of 100% (Fig. 2d). Such a high FVP is maintained during mode propagation. It should be noted that the coexistence of propagating GM1 and GM2 is a prerequisite for valley preservation. If the pump wavelength of the electric dipole is switched to 810 nm, the propagation of GM2 is prohibited. As a result, the modes launched by σ+ and σ− dipoles display similar profiles of GM1 (Fig. 2e), leading to the FVP being approximately equal to zero after a short distance of propagation (Fig. 2f).

The valley preservation in the WS_2-in-gap waveguide makes possible the selective routing of valleys. We construct a one-to-two valley router with one input channel and two output channels interconnected by a triangular structure (Fig. 3a). If K′ valley excitons are excited in the middle of the input channel, the launched waveguide mode will be routed to the output channel B, because the generated beating profiles have the electric field predominantly distributed on the lower side of the waveguide when entering into the triangle. The valley-path selectivity defined by $\mathrm{VS} = (I_A - I_B) / (I_A + I_B)$, is simulated to be −0.92 (see 'Numerical simulations' in the Methods), where I_A and I_B represent the optical intensities flowing into channels A and B (Supplementary Fig. 4), respectively. In the experiments, a pump laser is passed through a linear polarizer followed by a quarter-wave plate (QWP) and then focused onto the input channel by a 100× objective (see 'Optical characterization' in the Methods and Supplementary Fig. 5). The pump wavelength is 810 nm and the pump power is 22 mW, corresponding to a power density of 0.7 MW cm^{-2}. This results in σ+-polarized pump light inducing σ+-polarized TPL emission from WS_2. The direct coupling between the incident fundamental wave and the hybrid waveguide is prohibited by momentum mismatch (Supplementary Fig. 6). As shown in Fig. 3b, the experimental results reproduce well the simulations, where the output port B is considerably brighter than port A. Such an intensity contrast is more clearly revealed by the TPL spectra collected from the two ports (Fig. 3c). The VS is measured to be −0.46 ± 0.03. The quantum efficiency of TPL emission from the nanocircuits is measured and analysed in Supplementary Section 6. On the contrary, if σ− TPL emission is generated in the same position by σ− excitation, the generated waveguide mode will be routed to channel A, as confirmed by simulation and experimental results (Fig. 3d–f). The VS in this case is measured to be 0.44 ± 0.04. Such a large VS remains approximately stable for different pump intensities as shown in Supplementary Fig. 9.

The discrepancy between simulated and measured VSs is mainly attributed to the finite excitation spot. The pumped valley excitons have different intensities inside the excitation spot, while their path selectivities are also position dependent. Therefore, the effective selectivity measured from the two ports is a weighted average of the local selectivities with weights determined by the local intensities of excitons. The effective selectivity is calculated to be around −0.51 and +0.51 for σ+ and σ− excitations (see Supplementary Section 5), respectively. In two-dimensional transition-metal dichalcogenide monolayers, phonon-assisted intervalley scattering can lead to mixing of valley states, which seriously deteriorates the performance of valleytronic devices[21–23]. However, the close similarity between our measured valley selectivity and the calculated value (without considering intervalley scattering) implies that this effect has negligible impact on our system. In our case, the hybrid waveguide forms a nanocavity in the gap area with ultrasmall mode area and high Purcell factor. The effective mode areas A_{eff} of GM1 and GM2 are calculated to be 1.24×10^4 nm^2 and 1.47×10^4 nm^2, respectively, equivalent to $\lambda_0^2/32$ and $\lambda_0^2/27$, where λ_0 is the vacuum wavelength. Thus, the radiative exciton lifetime of WS_2 is largely reduced, while the valley polarization lifetime is almost unchanged. As a result, valley excitons are coupled to GMs through near-field non-radiative energy transfer, before the valley depolarization process occurs. Detailed analysis is included in Supplementary Section 8.

When a linearly polarized excitation is utilized, the K and K′ valleys are equally addressed, leading to nearly identical TPL signals from ports A and B (Fig. 3g). Furthermore, the excitation polarization can be continuously changed through the rotation angle φ of the QWP. Then, the VS approximately follows the relationship $\mathrm{VS} = 0.45 \times \sin(2\varphi)$ as shown in Fig. 3h. The dependence of VS on the geometric parameters of the hybrid waveguide is discussed in Supplementary Section 9. Specifically, the extreme values of VS (−0.46 and +0.44), corresponding to the valley pseudospin of electrons (K′ and K), can be harnessed as the binary digital elements of '0' and '1' to encode information. As a proof of concept, we have realized the encoding, transport and decoding of the word 'LOVE' as recorded in Supplementary Video 1. The retrieved

VS values for the capital letter 'E', whose ASCII and binary codes are '069' and '01000101', respectively, are plotted in Fig. 3i.

Based on the nanocircuit, we further demonstrate the function of valleytronic gyrators. As illustrated in Fig. 4a, K′ valley information loaded at one channel of the circuitry can only transport counter-clockwise to the next channel (1 → 2, 2 → 3, 3 → 1), while the clockwise circulation is largely prohibited. On the contrary, the transport of K valley information solely follows the clockwise sense (1 → 3, 3 → 2, 2 → 1) as shown in Fig. 4b. Such valley-dependent circulation is experimentally demonstrated in Fig. 4c,d. When $\sigma+$ excitation is applied to channel 1 to pump K′ valley excitons, the valley-carried optical signal obtained from port 2 is considerably stronger than that from port 3. However, if the $\sigma+$ pump light is illuminated on channel 2, the induced waveguide mode is not routed back to channel 1, but routed to channel 3. Such circulation direction is reversed for K valley excitons under $\sigma-$ excitation. The circulation directionality $CD = (I_c - I_{cc}) / (I_c + I_{cc})$ is calculated and indicated in Fig. 4c,d, where I_c and I_{cc} are the optical energies flowing in the clockwise and counter-clockwise directions, respectively.

In summary, we have reported a nanophotonic circuit to achieve the preservation and unidirectional circulation of the valley DOF, where a WS_2 monolayer is integrated into the gap area formed between TiO_2 nanowires and a gold film. Although the valleytronic functionalities showcased in this work are still at early stage, our proposed nanocircuit paves a never-explored avenue towards large-scale valleytronic networks. Moreover, it sheds new light on integrating valleytronics, spintronics and photonics on chip, enabling possibilities for hybrid spin-valley-photon systems.

Online content

Any methods, additional references, Nature Research reporting summaries, source data, extended data, supplementary information, acknowledgements, peer review information; details of author contributions and competing interests; and statements of data and code availability are available at https://doi.org/10.1038/s41565-022-01217-x.

References

1. Mak, K. F., McGill, K. L., Park, J. & McEuen, P. L. The valley Hall effect in MoS_2 transistors. *Science* **344**, 1489–1492 (2014).
2. Lee, J., Mak, K. F. & Shan, J. Electrical control of the valley Hall effect in bilayer MoS_2 transistors. *Nat. Nanotechnol.* **11**, 421–425 (2016).
3. Schaibley, J. R. et al. Valleytronics in 2D materials. *Nat. Rev. Mater.* **1**, 16055 (2016).
4. Vitale, S. A. et al. Valleytronics: opportunities, challenges, and paths forward. *Small* **14**, 1801483 (2018).
5. Wang, G. et al. *Colloquium*: Excitons in atomically thin transition metal dichalcogenides. *Rev. Mod. Phys.* **90**, 021001 (2018).
6. Lundt, N. et al. Optical valley Hall effect for highly valley-coherent exciton-polaritons in an atomically thin semiconductor. *Nat. Nanotechnol.* **14**, 770–775 (2019).
7. Ciarrocchi, A., Tagarelli, F., Avsar, A. & Kis, A. Excitonic devices with van der Waals heterostructures: valleytronics meets twistronics. *Nat. Rev. Mater.* https://doi.org/10.1038/s41578-41021-00408-41577 (2022).
8. Wolf, S. et al. Spintronics: a spin-based electronics vision for the future. *Science* **294**, 1488–1495 (2001).
9. Bhatti, S. et al. Spintronics based random access memory: a review. *Mater. Today* **20**, 530–548 (2017).
10. Bonilla, M. et al. Strong room-temperature ferromagnetism in VSe_2 monolayers on van der Waals substrates. *Nat. Nanotechnol.* **13**, 289–293 (2018).
11. Chen, Z. & Segev, M. Highlighting photonics: looking into the next decade. *eLight* **1**, 1–12 (2021).
12. Levy, J. S. et al. CMOS-compatible multiple-wavelength oscillator for on-chip optical interconnects. *Nat. Photonics* **4**, 37–40 (2010).
13. Cheben, P., Halir, R., Schmid, J. H., Atwater, H. A. & Smith, D. R. Subwavelength integrated photonics. *Nature* **560**, 565–572 (2018).
14. Fleury, R., Sounas, D. L., Sieck, C. F., Haberman, M. R. & Alu, A. Sound isolation and giant linear nonreciprocity in a compact acoustic circulator. *Science* **343**, 516–519 (2014).
15. Barzanjeh, S. et al. Mechanical on-chip microwave circulator. *Nat. Commun.* **8**, 953 (2017).
16. Scheucher, M., Hilico, A., Will, E., Volz, J. & Rauschenbeutel, A. Quantum optical circulator controlled by a single chirally coupled atom. *Science* **354**, 1577–1580 (2016).
17. Nagulu, A., Reiskarimian, N. & Krishnaswamy, H. Non-reciprocal electronics based on temporal modulation. *Nat. Electron.* **3**, 241–250 (2020).
18. Lee, D. et al. Hyperbolic metamaterials: fusing artificial structures to natural 2D materials. *eLight* **2**, 1–23 (2022).
19. Chen, P. et al. Chiral coupling of valley excitons and light through photonic spin–orbit interactions. *Adv. Opt. Mater.* **8**, 1901233 (2020).
20. Chen, Y. et al. Multidimensional nanoscopic chiroptics. *Nat. Rev. Phys.* **4**, 113–124 (2021).
21. Gong, S. H., Alpeggiani, F., Sciacca, B., Garnett, E. C. & Kuipers, L. Nanoscale chiral valley-photon interface through optical spin-orbit coupling. *Science* **359**, 443–447 (2018).
22. Chervy, T. et al. Room temperature chiral coupling of valley excitons with spin-momentum locked surface plasmons. *ACS Photonics* **5**, 1281–1287 (2018).
23. Sun, L. et al. Separation of valley excitons in a MoS_2 monolayer using a subwavelength asymmetric groove array. *Nat. Photonics* **13**, 180–184 (2019).
24. Gong, S.-H., Komen, I., Alpeggiani, F. & Kuipers, L. Nanoscale optical addressing of valley pseudospins through transverse optical spin. *Nano Lett.* **20**, 4410–4415 (2020).
25. Chen, P.-G. et al. Long-range directional routing and spatial selection of high-spin-purity valley trion emission in monolayer WS_2. *ACS Nano* **15**, 18163–18171 (2021).
26. Zeng, H., Dai, J., Yao, W., Xiao, D. & Cui, X. Valley polarization in MoS_2 monolayers by optical pumping. *Nat. Nanotechnol.* **7**, 490–493 (2012).
27. Mak, K. F., He, K., Shan, J. & Heinz, T. F. Control of valley polarization in monolayer MoS_2 by optical helicity. *Nat. Nanotechnol.* **7**, 494–498 (2012).
28. Cao, T. et al. Valley-selective circular dichroism of monolayer molybdenum disulphide. *Nat. Commun.* **3**, 887 (2012).
29. Xiao, J. et al. Nonlinear optical selection rule based on valley-exciton locking in monolayer ws_2. *Light Sci. Appl.* **4**, e366–e366 (2015).
30. Luo, Y. et al. Deterministic coupling of site-controlled quantum emitters in monolayer WSe_2 to plasmonic nanocavities. *Nat. Nanotechnol.* **13**, 1137–1142 (2018).
31. Wu, Z., Li, J., Zhang, X., Redwing, J. M. & Zheng, Y. Room-temperature active modulation of valley dynamics in a monolayer semiconductor through chiral Purcell effects. *Adv. Mater.* **31**, e1904132 (2019).
32. Oulton, R. F., Sorger, V. J., Genov, D. A., Pile, D. F. P. & Zhang, X. A hybrid plasmonic waveguide for subwavelength confinement and long-range propagation. *Nat. Photonics* **2**, 496–500 (2008).

Methods

Numerical simulations

All the simulations in this work are conducted using Lumerical FDTD software. The dielectric constant of TiO_2 is taken from spectroscopic ellipsometry data, while the permittivity of gold is taken from ref. [33]. The dielectric constant of SiO_2 is set as 1.42. Perfectly matched layer boundary conditions are employed to encircle the whole circuitry structure. The width and height of the waveguide are set as w = 240 nm and h = 100 nm. The thickness of the SiO_2 film is g = 20 nm. The central equilateral triangle has a side length of 1 μm. For simulating valley routing, a circular electric dipole is positioned 2 nm above the gold film and located 1 μm away from the entrance of the triangle to emulate the TPL emission of WS_2 excitons. A mesh size of 4 nm × 4 nm × 2 nm is utilized in the gap area.

Sample fabrication

The fabrication process of the nanophotonic circuit is illustrated in Supplementary Fig. 1. A 60-nm thick Au film with a 5-nm thick Cr adhesion layer is first deposited on a quartz substrate using electron beam evaporation. WS_2 monolayers grown on a sapphire substrate (SixCarbon technology, Shenzhen) are then transferred to the Au film with the help of polydimethylsiloxane (PDMS) and dilute HF solution. The PDMS is placed upside down over the WS_2 monolayers on the sapphire substrate and then diluted HF (2 vol%) solution is dripped into the gap between the sapphire surface and the PDMS layer to etch the sapphire surface for 10 min. After that, deionized water is dripped into the gap and it is rinsed three times in order to remove the residual HF solution. The PDMS–WS_2 can be naturally lifted off from the sapphire substrate and WS_2 monolayers are transferred to the PDMS. With the help of a home-built motorized transfer stage, WS_2 monolayers are transferred to Au film under the microscope. Then, a 20-nm thick SiO_2 film is deposited onto the WS_2/Au interface using electron beam evaporation.

TiO_2 nanowires are patterned using electron beam lithography. The polymethyl methacrylate (PMMA, 950,000 molecular mass) resist is spin-coated onto the SiO_2 film at a spin speed of 4,000 r.p.m. to give a 300-nm thick PMMA layer. The PMMA is then baked at 150 °C for 180 s to remove residual stress and solvent. After that we pattern the resist using electron beam lithography (Raith 150, electron acceleration voltage 20 kV) and develop it in solutions (AR 600-56, Allresist and isopropyl alcohol, Aladdin) to remove the exposed resist. Then, a 100-nm thick TiO_2 film is deposited using electron beam evaporation. Finally, the remaining PMMA resist is removed using acetone and only the TiO_2 nanowire is left.

Optical characterization

As illustrated in Supplementary Fig. 5, a mode-locked Ti:sapphire femtosecond laser centred at 810 nm (Vitara Coherent, 25 fs and 80 MHz) is used as the excitation source. The polarization is adjusted using a QWP (WPQ05M-808, Thorlabs). A home-built optical system is used to measure the TPL signal emitted from WS_2 monolayers. The fundamental beam is focused using an objective (100× and 0.9 numerical aperture, Olympus) to generate a small size of focal spot. The emitted signal is collected by the same objective lens and separated into two channels by a beam splitter. The channels are respectively directed to a complementary metal–oxide semiconductor camera (Prime 95B, Photometrics) and a spectrometer (Acton 2500i with Pixis CCD camera, Princeton Instruments). A 720 nm short-pass filter and a 600 nm long-pass filter are respectively introduced before the complementary metal–oxide semiconductor camera and the spectrometer, in order to filter the reflected fundamental beam and extract the TPL signal. For the spin-resolved photoluminescence measurement, the emitted TPL signal is extracted using a Glan-laser polarizer (GT10-A, Thorlabs) with a QWP (WPQW-VIS-4M, OptoSigma) at the visible band before the spectrometer.

Data availability

The raw data underlying the graphs of this paper are available via Figshare at https://figshare.com/articles/dataset/RAW_data_for_NNANO-22061298A.rar/20515695. Further data that support the findings of this study are available from the corresponding authors upon reasonable request.

References

33. Palik, E.D. *Handbook of Optical Constants of Solids* Vol. 3 (Academic Press, 1998).

Acknowledgements

Y.C. acknowledges support from the start-up funding of the University of Science and Technology of China and the CAS Talents Program. This work was supported by the National Natural Science Foundation of China (Nos. 12021004, 91850113, 11774115 and 11904271) and the Basic and Applied Basic Research Major Program of Guangdong Province (No. 2019B030302003). We thank the Center of Nano-Science and Technology of Wuhan University for their support in sample fabrication. This work was partially carried out at the USTC Center for Micro and Nanoscale Research and Fabrication. D.W. acknowledges support from the National Natural Science Foundation of China (No. 61927814). A.A. acknowledges financial support from the Air Force Office of Scientific Research with MURI grant no. FA9550-18-1-0379 and the Simons Foundation. C.-W.Q. acknowledges financial support from the National Research Foundation, Prime Minister's Office, Singapore under Competitive Research Program Award NRF-CRP22-2019-0006. C.-W.Q. is also supported by a grant (A-0005947-16-00) from the Advanced Research and Technology Innovation Centre (ARTIC).

Author contributions

Y.C. and C.-W.Q. conceived the idea and designed the experiments. K.W., P.L. and C.-W.Q. supervised the project. Y.C. conducted the simulations and theoretical analysis. S.Q., X.X and K.W. performed the experiments. Y.C., K.W., and C.-W.Q analysed the data. Y.C. drafted the paper with input from all authors.

Competing interests

The authors declare no competing interests.

Additional information

Supplementary information The online version contains supplementary material available at https://doi.org/10.1038/s41565-022-01217-x.

Correspondence and requests for materials should be addressed to Kai Wang, Peixiang Lu or Cheng-Wei Qiu.

Peer review information *Nature Nanotechnology* thanks Jorge Quereda and Xiaomu Wang for their contribution to the peer review of this work.